

Strong [OIII] λ 5007 emission line compact galaxies in LAMOST DR9: Blueberries, Green Peas and Purple Grapes

SIQI LIU ^{1,2} A-LI LUO* ^{1,2,3} HUAN YANG ^{4,5} SHI-YIN SHEN ^{6,7} JUN-XIAN WANG ^{4,8} HAO-TONG ZHANG ¹
ZHENYA ZHENG ^{6,7} YI-HAN SONG ¹ XIAO KONG ¹ JIAN-LING WANG ¹ AND JIAN-JUN CHEN^{1,2}

¹ CAS Key Laboratory of Optical Astronomy, National Astronomical Observatories, Beijing 100101, China

² University of Chinese Academy of Sciences, Beijing 100049, China

³ College of computer and Information Management & Institute for Astronomical Science, Dezhou University, Dezhou 253023, China

⁴ CAS Key Laboratory for Researches in Galaxies and Cosmology, University of Science and Technology of China, Chinese Academy of Sciences, Hefei, Anhui 230026, China

⁵ Las Campanas Observatory, Carnegie Institution of Washington, Casilla 601, La Serena, Chile

⁶ Key Laboratory for Research in Galaxies and Cosmology, Shanghai Astronomical Observatory, Chinese Academy of Sciences, 80 Nandan Road, Shanghai, 200030, China

⁷ Key Lab for Astrophysics, Shanghai, 200034, China

⁸ School of Astronomy and Space Science, University of Science and Technology of China, Hefei 230026, China

(Received; Revised; Accepted)

ABSTRACT

Green Pea and Blueberry galaxies are well-known for their compact size, low mass, strong emission lines and analogs to high- z Ly α emitting galaxies. In this study, 1547 strong [OIII] λ 5007 emission line compact galaxies with 1694 spectra are selected from LAMOST DR9 at the redshift range from 0.0 to 0.59. According to the redshift distribution, these samples can be separated into three groups: Blueberries, Green Peas and Purple Grapes. Optical [MgII] λ 2800 line feature, BPT diagram, multi-wavelength SED fitting, MIR color, and MIR variability are deployed to identify 23 AGN candidates from these samples, which are excluded for the following SFR discussions. We perform the multi-wavelength SED fitting with GALEX UV and WISE MIR data. Color excess from Balmer decrement shows these strong [OIII] λ 5007 emission line compact galaxies are not highly reddened. The stellar mass of the galaxies is obtained by fitting LAMOST calibrated spectra with the emission lines masked. We find that the SFR is increasing with the increase of redshift, while for the sources within the same redshift bin, the SFR increases with mass with a similar slope as the SFMS. These samples have a median metallicity of $12+\log(\text{O}/\text{H})$ of 8.10. The metallicity increases with mass, and all the sources are below the mass-metallicity relation. The direct-derived T_e -based metallicity from the [OIII] λ 4363 line agrees with the empirical N2-based empirical gas-phase metallicity. Moreover, these compact strong [OIII] λ 5007 are mostly in a less dense environment.

Keywords: galaxies: evolution – galaxies: emission line– catalogs: galaxies

1. INTRODUCTION

The Large sky Area Multi-Object Fiber Spectroscopic Telescope (LAMOST) (Wang et al. 1996; Su & Cui 2004), located at the Xinglong Observatory in Hebei Province northeast of Beijing, has an effective aperture of 4 m. Ensembling 4000 fibers, the LAMOST facility

can collect multiple spectra at the same time (Cui et al. 2012). The science goal for LAMOST extragalactic survey is to investigate the extragalactic objects for galaxies and QSOs (Zhao et al. 2012). Fig.1 demonstrates the our selected strong [OIII] λ 5007 emission line compact galaxies in the Galactic coordinates, which will be illustrated in Section 2.2 in detail.

Green Pea galaxies were first identified in the Galaxy Zoo project (Cardamone et al. 2009) by their unique compact size and green color caused by strong [OIII] λ 5007 emission lines. Cardamone et al. (2009)

Corresponding author: A-Li Luo

* lal@nao.cas.cn

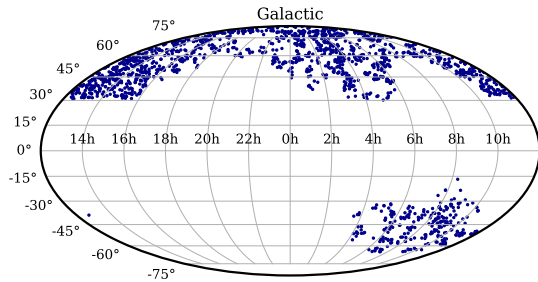


Figure 1. The sources in the Galactic coordinates, mainly around the North Galactic Cap (NGC) and the South Galactic Cap (SGC).

found 251 Green Pea galaxies from SDSS DR 7 by photometric color criteria, where 80 of the sources have spectroscopic data. Following studies have enlarged the sample size for the Green Pea galaxies. Izotov et al. (2011) contains 803 star-forming luminous compact galaxies (LCGs) with high $H\beta$ luminosities in the redshift range $z = 0.02 - 0.63$ from SDSS DR7 spectroscopic data. Jiang et al. (2019) contains 800+ Green Pea galaxies from the spectroscopic database of SDSS DR13 and use these samples to do direct T_e -based metallicity calibration.

Blueberry galaxies at $z < 0.05$ are the lowest mass young starburst galaxies (Yang et al. 2017) where the $[OIII]\lambda 5007$ emission line is located within the g -band and the $H\alpha$ emission line is located within the r -band. Purple Grape galaxies (Izotov et al. 2011; Brunner et al. 2020) where either that the $[OIII]\lambda 5007$ emission line is located in the i -band at $z > 0.36$ and the UV continuum is redshifted to the g -band, or the $[OIII]\lambda 5007$ is located in the g -band and the $H\alpha$ emission line is located in the i -band ($0.112 < z < 0.36$).

In this work, we compile a large catalog consisting of strong $[OIII]\lambda 5007$ emission line compact galaxies with 1694 spectra from LAMOST DR9 at the redshift range from 0.0 to 0.722. Among the sources 219 have SDSS spectra detections from SDSS DR16 (Blanton et al. 2017; Ahumada et al. 2020). Joint with multi-band photometry, we can systematically learn about the properties for these high SFR, compact galaxies spanning a wide range of redshift coverage.

In Section 2, we describe sample selection criteria, how we do the flux calibration of the LAMOST spectra and the multiwavelength dataset we use for following discus-

sions. In Section 3, we describe multi-wavelength SED fitting result, and how we identify the AGN candidates from the samples. In Section 4, we discuss the physical properties for these sources, including the stellar mass of the galaxies from spectral fitting, the SFR, the gas-phase metallicity, and the environment. In Section 5, we summarize the results addressed in this work.

In this work, we use *Wilkinson Microwave Anisotropy Probe* (WMAP) 9 cosmology (Hinshaw et al. 2013), AB magnitudes (Oke & Gunn 1983), Chabrier IMF (Chabrier 2003), and Bruzual & Charlot (2003) SPS models.

2. SAMPLE AND DATA

2.1. Sample

There are mainly two ranges that we select the strong $[OIII]\lambda 5007$ samples from the LAMOST DR9 of the extragalactic survey based on the color selection: from both dedicated or non-dedicated “Green Pea” targets of the input-catalog.

The dedicated “Green Pea” targets in the input catalog originate from the PI project of LAMOST extragalactic survey add-on program covering a large area of the North Galactic Cap and a strip in the South Galactic Cap. By now, 2309 spectra have been observed in LAMOST DR9¹

$$\begin{aligned} u - r &\leq 2.5, \\ r - i &\leq -0.2, \\ r - z &\leq 0.5, \\ g - r &\geq r - i + 0.5, \\ u - r &\leq 2.5(r - z). \end{aligned} \tag{1}$$

For the non-dedicated “Green Pea” targets in the input-catalog (by non-dedicated we mean that the initial purpose for observing this target was not intended for observing Green Pea galaxies, Blueberry galaxies or other compact emission line galaxies), we select extra 23 Blueberry galaxies (25 spectra), 19 Green Pea galaxies (19 spectra) and 2 Purple Grape galaxies (3 spectra) using the same color criteria in Equation 1, as displayed in Fig.2.

¹ <http://www.lamost.org/dr9/>. The initial color criteria determined from SDSS 12² *ugriz* photometry are as follows. For the sources in $z < 0.12$, where the $[OIII]\lambda 5007$ is located within the g -band, the criteria are two-fold: loose color criteria with $u - g \leq 0.3$, $r - g \leq 0.1$ and $i - g \leq -0.7$ but require the `type=3` to be galaxy; or no constraint on morphology but require strict color criteria with $u - g \leq 0.5$, $r - g \leq 0.5$. For the sources in $0.12 < z < 0.4$, where the $[OIII]\lambda 5007$ is located within the r -band, the criteria are displayed in Equation 1 (the same as Equations (1)-(5) in Cardamone et al. (2009)).

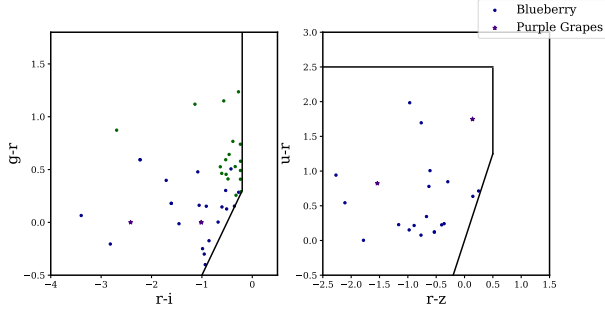


Figure 2. 44 newly selected Green Pea/Blueberry/Purple Grape galaxies samples from the color selection criteria. The green solid lines mark the color selection criteria from Cardamone et al. (2009) of Green Pea galaxies. There are 3 Blueberry galaxies and 1 Green Pea galaxy located at the left part of the left panel plot which are not displayed in this figure, and there are four Blueberry galaxies located at the left part in the right panel not displayed.

Next, we remove the sources with a large radius in r -band whose `petroRad_r` > 5 arcsec. We only keep the sources where the `mode` keyword is equal to 1 from the PhotoObjAll in SDSS DR13 which means primary object. Furthermore, we visually inspect the SDSS images and only keep the isolated sources. For the last step, we visually inspect each spectrum to ensure the strong [OIII] $\lambda 5007$ emission lines lie within the spectra and only keep the sources where the flux of [OIII] $\lambda 5007$ line is above 3×10^{17} erg/s/cm 2 .

Finally, 1547 in total strong [OIII] $\lambda 5007$ emission line compact galaxies with 1694 spectra are selected. LAMOST pipeline have classified these sources into four types: 1646 GALAXY, 3 STAR, 35 QSO and 14 Unknown.

Fig.3 shows the spectral redshift distribution of these samples. The majority of our sources are un-resolved

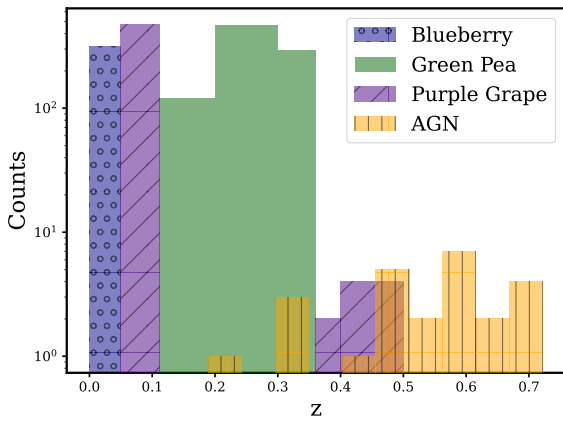


Figure 3. The spectral redshift distribution of the sources.

or barely resolved, where the Petrosian radius of the source is close to the FWHM of the PSF as displayed in Fig.4. We display our sources in the $u-r$ vs M_r color-magnitude diagram in Fig.5. As we have expected the majority of the strong [OIII] $\lambda 5007$ galaxies are located in the blue cloud region of the color-magnitude diagram under the division line defined in Baldry et al. (2004).

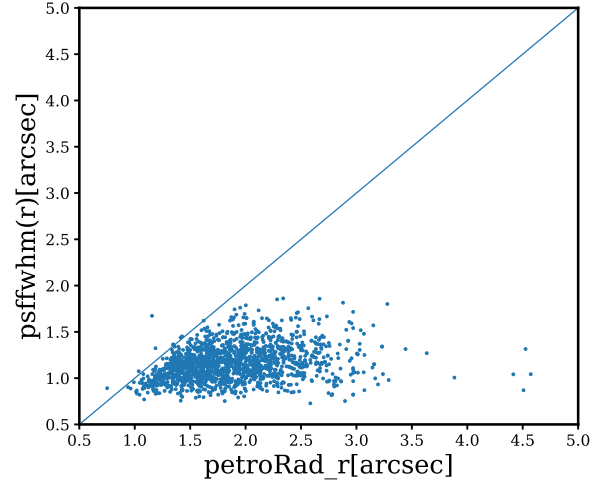


Figure 4. The scatter plot of the `petroRad_r` and `psffwhm(r)` of our strong [OIII] $\lambda 5007$ emission line compact galaxies.

All the sources within the redshift range within $0.59 < z < 0.73$ are AGN candidates, whose selection criteria will be discussed in Section 3.

2.2. LAMOST spectra flux calibration

The 16 LAMOST spectrographs are designed to have a theoretical resolution of $R = 1800$, covering the wavelength range from 3600 – 9000 Å. The blue portion spectrograph covers the wavelength range of 3690 – 5900 Å and the red portion spectrograph spans the wavelength coverage is 5700 – 9100 Å with 200 Å coverage overlap (Luo et al. 2012).

The response curves of the 16 spectrographs have been removed from LAMOST spectra, but the spectra flux is not physically calibrated (Du et al. 2016). We recalibrate the LAMOST spectra according to the SDSS gri photometry following Wang et al. (2018) as described below: LAMOST spectra are convolved with the SDSS gri filters (Fukugita et al. 1996) to obtain the synthetic magnitude for these three bands, then compared with the SDSS photometric magnitude. A zeroth-order or first-order polynomial is used to fit the magnitude difference array and apply this correction to the LAM-

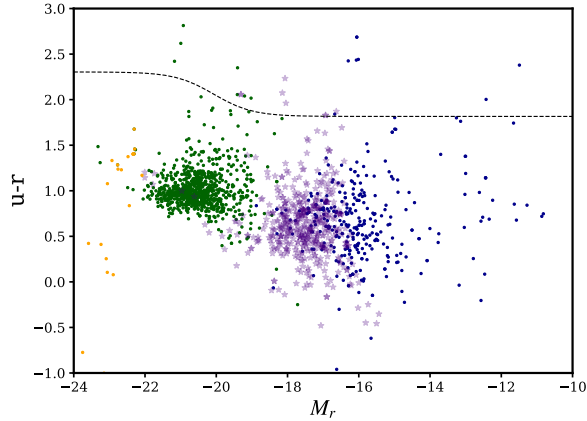


Figure 5. Color-magnitude diagram of the strong [OIII] λ 5007 emission line compact galaxies. The absolute magnitude of the r -band and the $u-r$ color are k -corrected with Chilingarian et al. (2010); Chilingarian & Zolotukhin (2012). The dark blue dots mark the Blueberry galaxies, the dark green dots mark the Green Pea galaxies, the indigo stars mark the Purple Grape galaxies, and the orange dots mark the spectroscopically-confirmed AGNs. The majority of our samples locate in the blue cloud region of the color-magnitude diagram, below the dividing line defined by Baldry et al. (2004) between the red sequence and the blue cloud.

OST spectra. An example of the flux calibration result is shown in Fig.6.

For some sources that the LAMOST data reduction pipeline did not calculate their redshift, we need to determine the redshift by fitting the emission lines.

2.3. UV and MIR photometry

We cross-match the sources with the *GALAXY EVOLUTION EXPLORER* (GALEX) mission (Martin et al. 2005) the revised GALEX catalog of UV sources (GU-Vcat_AIS) from GR6+7 (which contains 82,992,086 sources) (Bianchi et al. 2017; Bianchi et al. 2017) using a radius of 3 arcsec and have obtained 1266 cross-matched results.

The *Wide-field Infrared Survey Explorer* (WISE) (Wright et al. 2010) mission has conducted a MIR survey with 3.4, 4.6, 12, and 22 μ m band-passes. We cross-match our sources in 10 arcsec separation with the All-WISE source catalog, which contains photometry and astrometry of over 747 million objects. Although this separation is large, we have eye-checked every source to ensure there is no contamination source within the search radius. We perform the following criteria in SNR and χ^2_ν space to remove the fake objects from the cross-matched results, as Koenig & Leisawitz (2014) Section

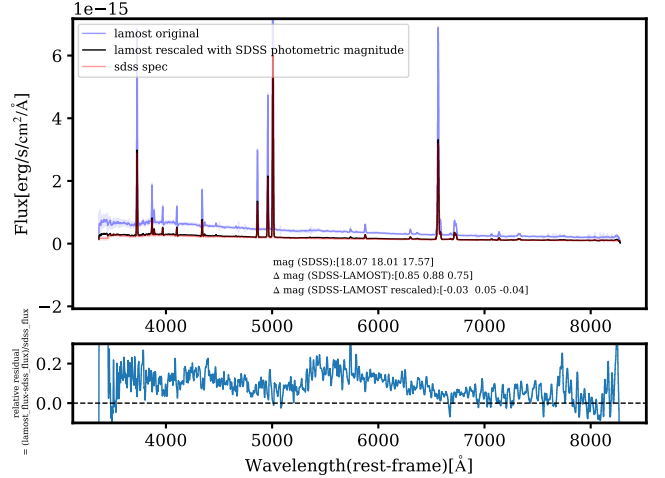


Figure 6. An example of flux calibration of LAMOST spectra. In the upper panel, we plot the original LAMOST spectra before flux calibration (transparent blue curve), the LAMOST spectra that are re-calibrated with SDSS gri photometric magnitudes (black curve), and the SDSS spectra (red curve). In the lower panel, we plot the relative residual = (LAMOST_flux - SDSS_flux) / SDSS_flux. We also mark the 0 level with the horizontal line. We have smoothed both the LAMOST spectra and the SDSS spectra with a kernel of 3.

3.1.1 has performed. There are 138 sources after cross-matching with WISE.

We cross-match with *Spitzer Space Telescope* (Werner et al. 2004) data with Spitzer Enhanced Imaging Products (SEIP) using 3 arcsec radius separation and obtained 32 sources that have detections in Infrared Array Camera (IRAC) (Fazio et al. 2004) and 37 that have detections in Multiband Imaging Photometer for Spitzer (MIPS) (Rieke et al. 2004). We use Spitzer and WISE photometry for multi-band SED fitting as described in the next subsection.

3. MULTIWAVEBAND SED FITTING AND AGN CANDIDATES

3.1. CIGALE SED fitting

We fit the sources with multi-wavelength photometry with CIGALE (Burgarella et al. 2005; Noll et al. 2009; Boquien et al. 2019) trying to use the full photometric data for the 138 sources. As described in the above section, however, GALEX (97 sources) and Spitzer (5 sources) data are available for some of them in addition to SDSS and WISE photometry for the 138 sources. For the configuration of the SED creation modules, we use the delayed- τ star formation history, BC03 (Bruzual & Charlot 2003), Chabrier IMF (Chabrier 2003), nebular emission lines, dust attenuated modified starburst model, the dust emission model from Casey (2012), and

the Fritz et al. (2006) AGN model. An example of the CIGALE SED fitting result is shown in Fig.7.

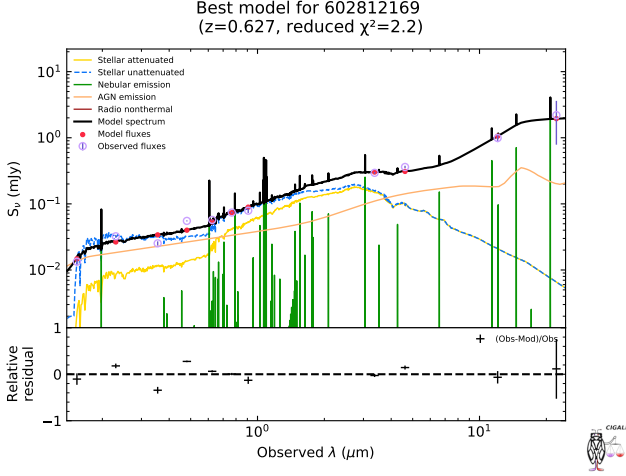


Figure 7. CIGALE SED fitting with GALEX, SDSS *ugriz* and WISE *W*₁ to *W*₄ photometry. The dust temperature from the best-fitting result for this source is 325K and the AGN fraction is 20%.

3.2. AGN candidates

We identify AGNs from our samples using five aspects: (1) the existence of [MgII]λ2800 emission line in the optical spectra (as addressed in Section 2.1), (2) the BPT diagram, (3) AGN fraction determination from CIGALE multi-wavelength SED fitting, (4) MIR color, and (5) MIR variability.

For the optical spectra, we spectroscopically confirm 19 AGNs with 21 spectra from LAMOST DR9 with the existence of [MgII]λ2800 emission lines. We display the stacked spectra with three-epoch [MgII]λ2800 detections in Fig.8, and name the source by its LAMOST designation J162736.10+56225.8, where we have three spectra from LAMOST.

Using the BPT diagram (Baldwin et al. 1981; Veilleux & Osterbrock 1987) we classify the galaxies into different spectral types according to the definitions in Kewley et al. (2001); Kauffmann et al. (2003); Kewley et al. (2006). There are 1423 galaxies (1547 spectra) that are classified as star-forming galaxies, 16 galaxies (16 spectra) as composite, and 71 galaxies (73 spectra) as AGN. We plot the distribution for these galaxies in the BPT diagram in Fig.9. We do not consider all the sources classified as AGN through the BPT diagram are real AGN sources as the majority of the sources are located in the upper left region of the diagram, where the high ionization is caused by the high [OIII] lines excited from the star-forming region, not the nuclear region. On the other hand, there might be AGN contaminants located

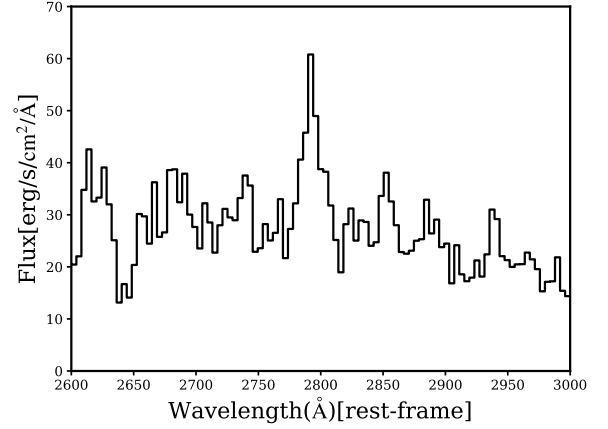


Figure 8. The stacked spectra of [MgII]λ2800 lines for three epochs with the AGN candidate LAMOST designation J162736.10+56225.8.

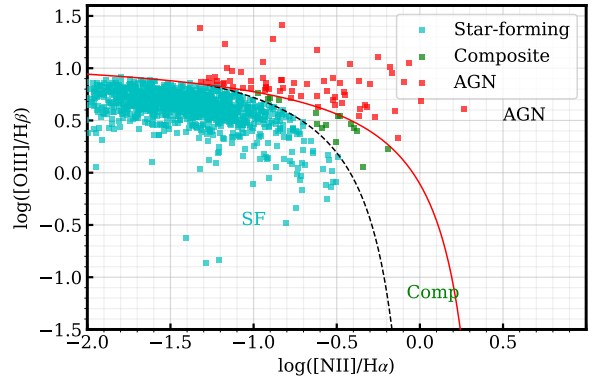


Figure 9. The BPT diagram of the strong [OIII]λ5007 emission line compact galaxies. This figure use the plotting routine in Cherinka et al. (2019).

in the SF region especially in the low-metallicity regime as addressed in Harish et al. (2021).

We have confirmed the existence of AGNs from the CIGALE multi-band photometry fitting result, where we use Fritz et al. (2006) model. Among the 138 sources that have multi-wavelength photometry, we have 2 sources where the AGN fraction is over 20%. An example of the SED fitting result is shown in Fig.7. For the MIR color selection, we follow the criteria in Jarrett et al. (2011) Equation 1 and have obtained 23 AGN candidates under this criteria. Multi-epoch exposures in the WISE catalog can be obtained from AllWISE Multiepoch Photometry Table and NEOWISE-R Single-Exposure Source (L1b) Source Table. Some filters are applied to select out the reliable detections in the good quality frames, explained in detail in the Explanatory

Supplements³. The light curves of the selected sources are displayed in Fig.10 and Fig.11. There are 23 sources with the $r_{12} > 0.6$ that meet the criteria in Harish et al. (2021) as MIR variables and cover the WISE and NEO-WISE detections of at least 9 epochs.

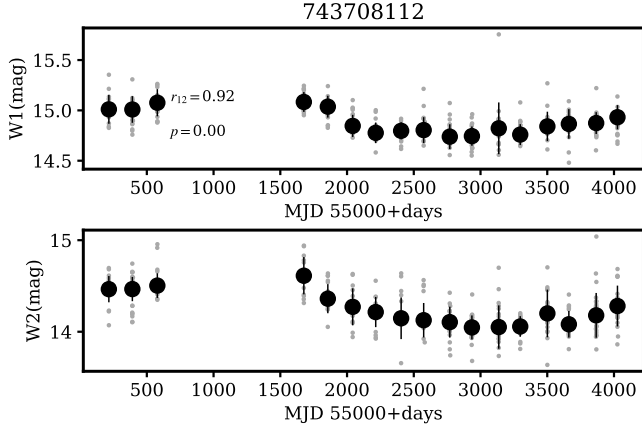


Figure 10. The light curve of one AGN candidate of W_1 (upper panel) and W_2 (lower panel), where the title marks the obsid from LAMOST. The Pearson r_{12} correlation is 0.93 with a p-value of 0.0. The single exposure magnitudes are marked with gray scatter points, where the median value and the standard deviation of the exposures from the same epoch within 60 days are marked with black error bars.

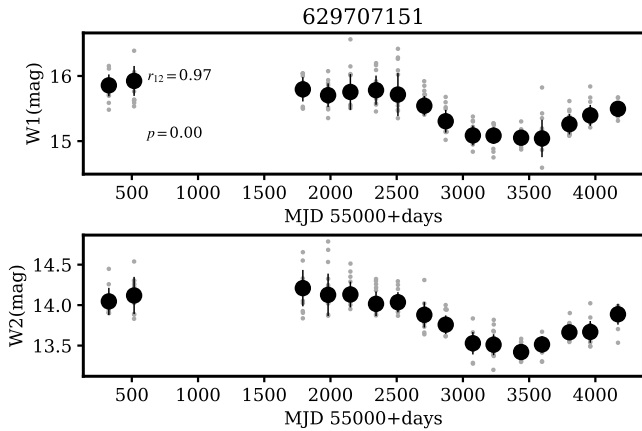


Figure 11. Same as in Fig.10 but for LAMOST obsid 629707151, where the Pearson r_{12} correlation is 0.97.

Furthermore, we have identified a strong X-ray emission source from the strong [OIII] λ 5007 emission

line galaxies after cross-matching with 4XMM-Newton DR11 (Webb et al. 2020; Traulsen et al. 2020). This source has the EPIC (indicates parameters combined from those from the available cameras) broadband energy at 0.2 - 12.0 keV of 1.033×10^{43} erg/s, which is higher than the luminosity of the AGNs in nearby galaxies addressed in Maitra et al. (2019). The $L_{0.5-4.5\text{keV}} = 9.27 \times 10^{42}$ erg/s higher than the AGN identification criteria for X-ray source in Section 4.4 of Xue et al. (2011) that a source with an intrinsic X-ray luminosity of $L_{0.5-8\text{keV}} = 3 \times 10^{42}$ erg/s is identified as a luminous X-ray AGN. Located at $z = 0.6022$, this source has the EP 9 broad-band energy covering the energy range of 0.5 - 4.5 keV in the observed frame with $L_{0.8-7.2\text{keV}} = 9.26 \times 10^{42}$ erg/s, which is a lower limit for the $L_{0.5-8\text{keV}}$. The SFR is from the FUV flux is $33.27 M_{\odot}/\text{yr}$ and $L_{0.5-8\text{keV}}/\text{SFR} > 41.44$. Comparing this source with the Brorby et al. (2016) $L_{0.5-8\text{keV}}/\text{SFR}$ level of 39.85 with a scatter of 0.25 dex, which is already higher than the Mineo et al. (2012) relation of 39.59, our source is much higher.

We summarize the sources that have been identified as AGNs with over four of the methods mentioned above in Table 1. 12 galaxies that have been identified with three the methods (8 identified by [MgII] λ 2008 emission lines, MIR color and MIR variability, and 4 galaxies identified with BPT diagram, MIR color, and MIR variability). For the galaxies that are identified with one or two methods, there are 11 spectra (9 galaxies) that have been identified with the existence of [MgII] λ 2800 line. We consider all the sources that are identified as AGNs with more than 3 methods or have been identified with the existence of [MgII] λ 2800 line as AGN candidates and exclude these 25 spectra (23 galaxies) from the star formation rate discussions in the following section.

4. PHYSICAL PROPERTIES

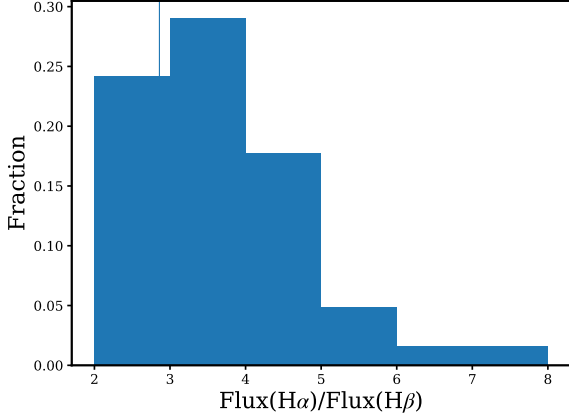
4.1. Color excess from the Balmer decrement

To ensure the quality of the flux ratio measurement, we select the sources at $0.173 \leq z \leq 0.385$ where both the $H\alpha$ and the $H\beta$ emission line locate within the red portion of the spectrograph. To ensure the validness of the detection, we apply a SNR cut (median value of the flux over the flux error of the $H\beta$ region) over 3 to select the sources. 62 spectra satisfy this criterion, and their flux ratio are displayed in Fig.12. We measure the color excess of the galaxies from the flux ratio of the $H\alpha$ to $H\beta$ assuming the Case B recombination with the intrinsic line ratio of 2.86. The color excess from the

³ <https://wise2.ipac.caltech.edu/docs/release/neowise/expsup/sec2.3.html> and <https://wise2.ipac.caltech.edu/docs/release/allwise/expsup/sec3.2.html>. Here we select the sources with `quality_score>0`, `qi_fact>0`, `saa_sep>0`, `moon_masked=0`, `cc_flags=0`, `w1rchi2_ep<2` and `w2rchi2_ep<2`.

Table 1. AGN candidate identified with over 4 criteria

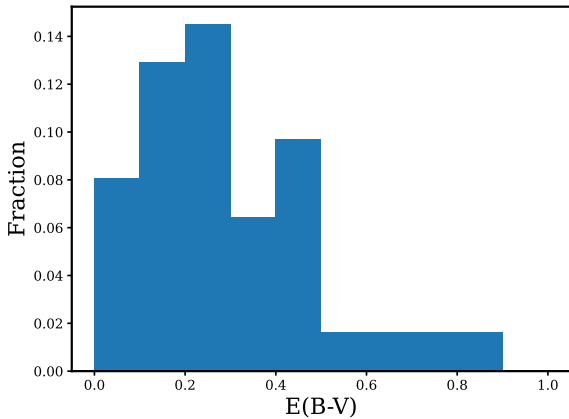
LAMOST designation	[MgII] λ 2008	BPT	CIGALE AGN fraction	MIR color criteria	MIR variability
J234141.49+140028.1	1 time	SF	0.20	in	$N_{ep} = 17, \sigma_1 > 0, \sigma_2 > 0, r_{12} = 0.64,$
J021459.09-014459.2	1 time	SF	0.21	in	$N_{ep} = 17, \sigma_1 > 0, \sigma_2 > 0, r_{12} = 0.61,$

**Figure 12.** The distribution of the flux ratio of $H\alpha/H\beta$.

flux ratio is calculated with:

$$E(B - V)_{\text{gas}} = \frac{\log_{10}[(f_{H\alpha}/f_{H\beta})/2.86]}{0.4 \times [k(H\beta) - k(H\alpha)]}, \quad (2)$$

where $k(H\alpha) = 3.33$ and $k(H\beta) = 4.6$ as Jiang et al. (2019). We assume that the nebular gas in these galaxies emit at $T = 10^4\text{K}$ and $n_e = 10^4\text{cm}^{-3}$. We show the distribution of the color excess in Fig.13. As is discussed

**Figure 13.** The distribution of the color excess determined from Equation 2.

in Section 4.1 in Cardamone et al. (2009), some of the

sources have a flux ratio below 2.86, we contribute this to the uncertainties in flux calibration and low extinction and manually set their color excess to be 0.

4.2. Mass and SFR

The main goal for this subsection is to investigate the mass-metallicity relation and compare the SFR derived from $H\alpha$ emission line and the FUV. We use 262 spectra (252 galaxies) with valid Starlight spectral fitting results for deriving the mass-metallicity relation, among which 4 are AGN candidates, 67 spectra (64 galaxies) are Blueberry galaxies, 123 spectra (116 galaxies) are Purple Grape galaxies ($0.05 \leq z < 0.112$), and 68 spectra (68 galaxies) are Green Pea galaxies. We use 24 samples with positive color excess from the previous subsection and FUV detection from GALEX to derive the extinction corrected SFR.

To derive the physical properties for these sources (Cid Fernandes et al. 2005; Mateus et al. 2006), we fit the re-calibrated LAMOST spectra with the emission lines masked. The fitting procedure is based on a base set of 45 spectra of three metallicities and 15 ages, with the stellar population model based on the BC03 high resolution spectra, and the Calzetti et al. (2000) extinction curve. The initial values of the velocity shift is set to be $v_0 = 0.0$ km/s, and the velocity dispersion is of $v_d = 150.0$ km/s. We only consider the Starlight fitting of the LAMOST spectra a valid fitting result, where $\frac{\chi^2}{N(\lambda_{\text{eff}})} < 0.2$, $\text{adev} < 30$ and $\text{SNR}(6000\text{\AA} < \lambda_{\text{rest-frame}} < 6500\text{\AA}) \geq 2.0$ and have obtained 262 sources. Fig.14 displays an example of Starlight SED fitting result.

Fig.15 demonstrates the relation of the stellar mass of the galaxies derived from Starlight with SFR (measured from the $H\alpha$ luminosity without extinction correction) (Dopita & Ryder 1994; Kennicutt 1998; Panuzzo et al. 2003; Dopita 2005; Kennicutt & Evans 2012). We separate the strong [OIII] λ 4363 emission compact galaxies into Blueberry galaxies, Green Pea galaxies, and Purple Grape galaxies, and compare the mass-SFR relation for these three sets of samples with the SFMS Within each redshift bin, we separate the sources into several mass bins and calculate the median value and the standard deviation of the mass and metallicity for the sources within

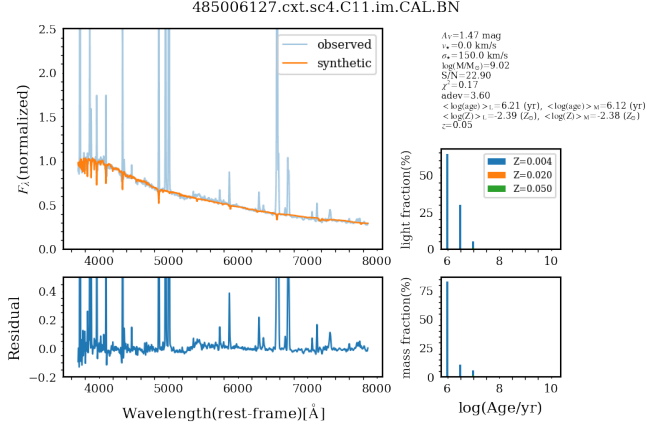


Figure 14. Example Starlight SED fitting result.

this mass and redshift bin. The main sequence SFR- M_*

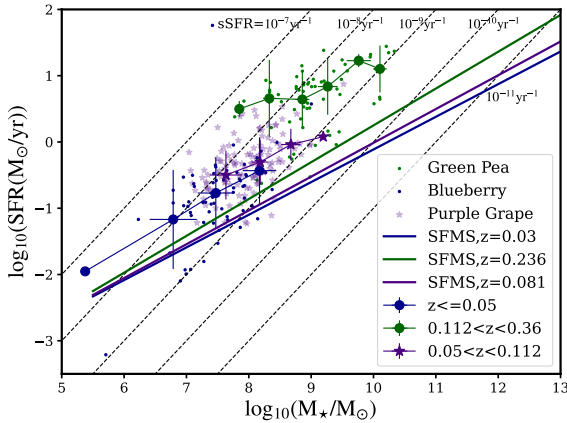


Figure 15. The stellar mass vs. star formation rate (SFR) for our selected strong [OIII] λ 5007 samples. Blueberry, Green Pea, and Purple Grape galaxies are marked with corresponding colors. We also mark the Star-Forming Main Sequence (SFMS) relation from Speagle et al. (2014) at different redshifts with dark blue ($z = 0.03$), dark green ($z = 0.236$) solid lines, and indigo lines ($z = 0.081$, we only have Purple Grape galaxies with Starlight derived mass in the $0.05 \leq z < 0.112$ redshift bin). The majority of our samples have a higher SFR region compared with the SFMS.

relation from Speagle et al. (2014) is as follows:

$$\log \text{SFR}(M_*, t) = (0.84 \pm 0.02 - 0.026 \pm 0.003 \times t) \log M_* - (6.51 \pm 0.24 - 0.11 \pm 0.03 \times t), \quad (3)$$

where t is the age of the universe in Gyr. Similar to the discussions in Section 4.4 in Cardamone et al. (2009), our strong [OIII] λ 5007 samples have much higher sSFR at this redshift range, where typically for the galaxies at $z \sim 0.2$ the sSFR is around 10^{-9}yr^{-1} (Brinchmann et al. 2004; Bauer et al. 2005).

With the H α emission line measurement result and the FUV flux, we intend to use this sample to check if the SFRs derived from these two indicators agree. The calculation of the SFR from the recombination emission lines (24 spectra which do not have H α spectral coverage are dropped out) and FUV flux follow the relation defined in Hao et al. (2011); Murphy et al. (2011); Kennicutt & Evans (2012), where the corresponding parameters are in Table 2:

$$\log \dot{M}_* (\text{M}_\odot \text{year}^{-1}) = \log L_x - \log C_x. \quad (4)$$

Table 2. Star Formation rate calibrations

Band	L_x units	$\log C_x$
FUV	$\text{ergs s}^{-1} (\nu L_\nu)$	43.35
H α	ergs s^{-1}	41.27

As discussed in Section 4.2, we convert from $E(B-V)$ to A_V using $A_V = R_V \times E(B-V)$ to the emission lines for the 62 high H β SNR galaxies, under the assumption of Calzetti et al. (2000) extinction curve and $R_V = 3.1$. Within these 62 samples, 36 samples are with positive color excess. 24 out of the 36 samples have GALEX FUV detections. Fig.16 illustrates the comparison of SFR without extinction correction (left panel) and after extinction correction (right panel) with these 24 samples.

4.3. Gas-phase metallicity

In this subsection, we first show the distribution of metallicity measured from the N2-based method with 1337 spectra, where the [NII] λ 6585 emission line is covered within the spectral range. Then we demonstrate the mass-metallicity relation of 252 sources that have Starlight-derived mass and the N2-based metallicity. Furthermore, we discuss the gas-phase metallicity calculated from the empirical N2-based method and the direct T_e -based method with 21 galaxies whose specific flux of the [OIII] λ 4363 emission lines are above $8.85 \times 10^{38} \text{erg/s/\AA}$, where the detection of [OIII] λ 4364 is rare (Gao et al. 2017).

We use the N2-based method (van Zee et al. 1998; Pettini & Pagel 2004; Marino et al. 2013) to empirically calculate the gas-phase metallicity. Because the two lines used in this method are close, thus less prone to the flux calibration error. The definition for this index is as follows:

$$\text{N2} = \log_{10}([\text{NII}]\lambda 6585/\text{H}\alpha), \quad (5)$$

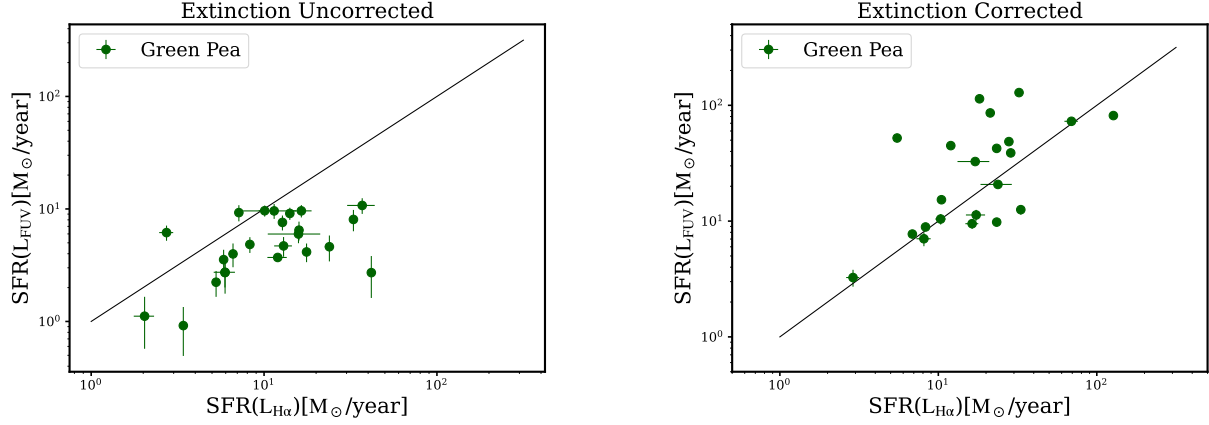


Figure 16. SFR ($H\alpha$) vs SFR (FUV). The black solid line marks the linear relation. The left panel shows the SFR without attenuation correction and the right panel shows the SFR with attenuation correction.

and this index can be converted to gas-phase metallicity with the following relation:

$$12 + \log(O/H) = 8.90 + 0.57 \times N2. \quad (6)$$

Fig. 17 displays the distribution of the N2-based method derived gas-phase metallicity. The gas-phase metallicity is higher than that of the pure Blueberry galaxies (Yang et al. 2017), similar to that of Cardamone et al. (2009).

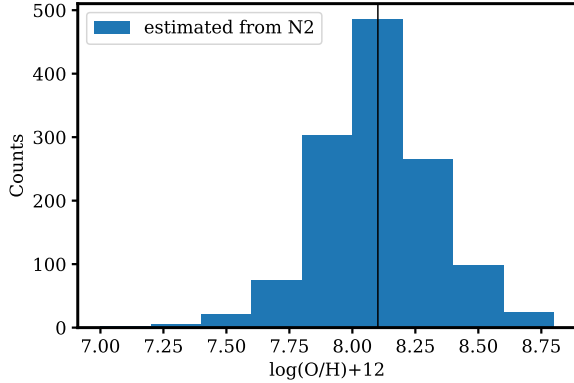


Figure 17. Gas-phase metallicity estimated from the N2-based method. We mark the median value of the metallicity distribution with the vertical line where $12 + \log(O/H) = 8.10$, about 0.26 solar metallicity.

We show the distribution of the mass-metallicity relation in Fig. 18. We separate 248 galaxies (258 spectra), which consist of 64 Blueberry galaxies (67 spectra), 68 Green Pea galaxies (68 spectra), and 116 Purple Grape galaxies (123 spectra) into seven mass bins and calculate the median value and the standard deviation of the

mass and metallicity for the sources within this mass bin.

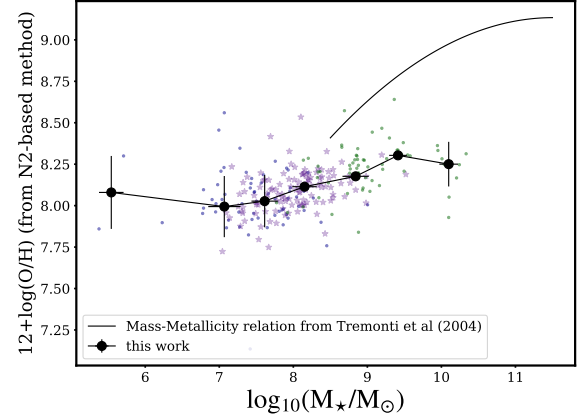


Figure 18. The mass-metallicity relation of 258 spectra with valid Starlight mass measurement. The blue dots mark the measurements from the Blueberry galaxies, the indigo stars mark the measurements from the Purple Grape galaxies at $0.05 \leq z < 0.112$ and the green dots mark the measurements from the Green Pea galaxies. We separate the whole sample into seven mass bins and mark the median value and the standard deviation of the mass and metallicity with black error bars. The black solid curve on the top right is from Tremonti et al. (2004).

We demonstrate that the metallicity increases with the mass by comparing the points, with the smallest mass bin and the largest mass bin excluded where are fewer data points in these two mass bins. All of these strong $[OIII]\lambda 4363$ emission line compact galaxies are below the Tremonti et al. (2004) mass-metallicity relation.

Besides the empirical method to calculate the gas-phase metallicity, there is also the direct T_e -based method. However, the auroral [OIII] λ 4363 line is not easy to detect. In this work, 21 galaxies whose specific flux of the [OIII] λ 4363 emission lines are above $8.85 \times 10^{38} \text{erg/s/\AA}$ are used to test the direct T_e -based method to calculate the electron temperature and the metallicity referring to Izotov et al. (2006) Section 3.1 and Jiang et al. (2019). The purpose of this discussion is to show that we have detected the auroral [OIII] λ 4363 emission line, which increases the samples of detections in LAMOST (Gao et al. 2017), and to demonstrate the current N2-based empirical metallicity relation and direct T_e -based metallicity relation in Jiang et al. (2019) are in agreement within $1-\sigma$ level.

This approach assumes two electron temperatures for O^+ and O^{++} in a two-zone photo-ionization model. We calculate the O^{++} electron temperature with the following equation, (as in Izotov et al. (2006) Equations (1) and (2)):

$$t = \frac{1.432}{\log[(\lambda 4959 + \lambda 5007)/\lambda 4363] - \log C_T}, \quad (7)$$

where $t = 10^{-4}T_e(\text{OIII})$, and

$$C_T = (8.44 - 1.09t + 0.5t^2 - 0.08t^3) \frac{1 + 0.0004x}{1 + 0.044x}, \quad (8)$$

where $x = 10^{-4}N_e t^{-0.5}$. We estimate electron temperature of [OII] for the low-metallicity situation in Izotov et al. (2006) Section 3.1 Equation (14) as follows:

$$T_e(\text{OII}) = -0.577 + T_e(\text{OIII}) \times (3.065 - 0.498T_e(\text{OIII})). \quad (9)$$

This is also the method that Jiang et al. (2019) uses for calculation, and they state that their measurement of the oxygen abundance depends little on the relation between T_2 and T_3 . Similarly, we use the term $T_2 = 10^{-4}T_e([\text{OII}])$ and $T_3 = 10^{-4}T_e([\text{OIII}])$ for clarity. Our spectra do not cover the [SII] λ 6717 or [SII] λ 6731 emission lines. The derived N_e is always smaller than 10^3cm^{-3} , and as in Jiang et al. (2019) $N_e = 10, 100$ or 10^3cm^{-3} the results do not vary much. We use $x = 0$ for our calculations.

With the Equations (3) and (5) in Izotov et al. (2006), we calculate the ionic abundances as follows:

$$12 + \log \frac{\text{O}^+}{\text{H}^+} = \log \frac{\lambda 3727}{\text{H}\beta} + 5.961 + \frac{1.676}{T_2} - 0.40 \log T_2 - 0.034T_2 + \log(1 + 1.35x), \quad (10)$$

and

$$12 + \log \frac{\text{O}^{2+}}{\text{H}^+} = \log \frac{\lambda 4959 + \lambda 5007}{\text{H}\beta} + 6.200 + \frac{1.251}{T_3} - 0.55 \log T_3 - 0.014T_3, \quad (11)$$

Because the majority of the ions of oxygen are O^+ and O^{2+} , we use $\text{O}/\text{H} = \text{O}^+/\text{H} + \text{O}^{2+}/\text{H}$ to determine oxygen abundance. Fig. 19 demonstrates the comparison of the gas-phase metallicity estimated from the N2-based method and the direct T_e -based method. We calculate the error bars in Fig 19 by the Monte Carlo method. For the error bars in the N2-based metallicity, we generate 100 realizations for each source within the wavelength range of 6500–6640 \AA with the flux error from the rescaled LAMOST spectra, and measure the [NII] λ 6585 line and the $\text{H}\alpha$ line flux for each realization. We calculate the N2-based metallicity for each realization and use the standard deviation from 100 realizations as the error bar for that source. For the error bars in the direct T_e -based method, similarly, we generate 100 realizations for each source but in a tighter wavelength range 4320 – 4383 \AA and measure the [OIII] λ 4363 line only for each realization. We note that 15 out of 21 sources locate on the black line within $1-\sigma$ region. This verifies that the current N2-based empirical metallicity relation and the direct T_e -based metallicity relation in Jiang et al. (2019) are in agreement within $1-\sigma$ level.

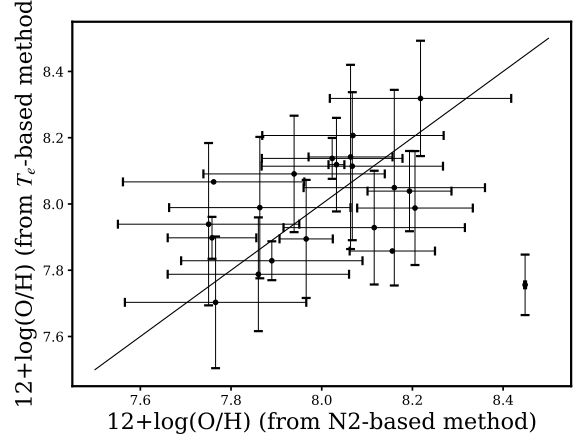


Figure 19. The relation of the derived gas-phase metallicity from the N2-based method (x-axis) and the direct T_e -based method (y-axis) is based on our 21 [OIII] λ 4363 samples. Adopting $12 + \log(\text{O}/\text{H}) = 8.69$ as in Allende Prieto et al. (2001), these 21 samples are all with sub-solar metallicities.

4.4. Environment

We identify a parent sample of comparison star forming galaxies from the “emissionLinesPort” catalog (Thomas et al. 2013) whose spectroscopic classification is ‘Galaxy’, the BPT classification is ‘star-forming’ and cover the same redshift range as our Blueberry galaxies ($z \leq 0.05$), Purple Grape galaxies ($0.05 < z \leq 0.112$ and

$0.36 \leq z < 0.59$), Green Peas ($0.112 \leq z < 0.36$). We ensure the parent comparison sample covers the same mag- z space as our selected samples in the r -band as displayed in the following plot. The Neighbors table from SDSS16 provides the angular separation to the nearby objects within 0.5 arc minutes. We only consider the primary detections as the valid neighbors. We calculate the projected linear separation between our source and all the valid neighbors by multiplying the angular separation from the Neighbors table with the luminosity distance at the redshift of our strong [OIII] λ 5007 emission line compact dwarf galaxies. We consider the smallest linear separation as the distance to the nearest neighbor. We display the distance for our samples to the nearest neighbor in different redshift bins in Fig.20.

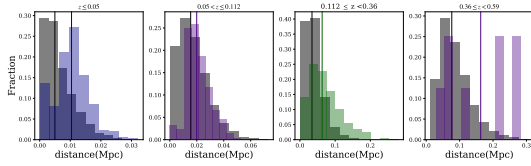


Figure 20. The histogram of the distance to the nearest neighbor. The colored histogram displays the strong [OIII] λ 5007 samples while the gray histogram shows the parent comparison star forming galaxies sample selected from SDSS. We mark the median values (strong [OIII] λ 5007 samples, parent SFGs) of the two distributions with vertical lines of corresponding colors.

We also perform the Komogorov-Smirnov test for these four sets of comparisons, and the p-value between the distance to the nearest neighbor of the parent sample and our selected sample in four redshift bins are all smaller than 0.05. Therefore, it is apparent that the strong [OIII] λ 5007 samples are further away from the nearest neighbor compared with typical star forming galaxies.

5. RESULT

We have selected 1547 unique strong [OIII] λ 5007 emission line compact galaxies with 1694 spectra⁴ from LAMOST DR9. 1342 galaxies are observed spectroscopically for the first time. Our samples enlarge the current samples of luminous compact galaxies, Green Pea galaxies, and Blueberry galaxies. The following LAMOST extragalactic survey will keep providing large amount of spectra for these targets and provide duplicate detections for the same source helpful for observing the line variability.

We have confirmed 23 AGNs candidates (25 spectra) from this strong [OIII] λ 5007 emission line compact galaxies by LAMOST optical spectra, BPT diagram, CIGALE SED fitting, MIR color, and MIR variability.

Our samples show that strong [OIII] λ 5007 emission-line galaxies have higher SFR compared with the main-sequence star formation rate. The SFR from the FUV luminosity with the H α luminosity agrees with the coefficients after extinction correction from Kennicutt & Evans (2012). From the mass-SFR plot, we show that with the increase of redshift, the SFR is increasing. For the sources within the same redshift bin, the SFR increases with mass with a similar slope as the SFMS.

For the gas-phase metallicity for these samples, these samples have a median metallicity of $12+\log(\text{O}/\text{H})$ of 8.10. In the mass-metallicity plot, all the sources are below the Tremonti et al. (2004) mass-metallicity relation. The metallicity increases with mass. 21 galaxies are found with [OIII] λ 4363 emission lines. The direct T_e -based metallicity measurement result is in agreement with the N2-based metallicity result.

Lastly, Strong [OIII] λ 5007 emission-line galaxies are in a less dense environment.

ACKNOWLEDGEMENTS

This work is supported by National Science Foundation of China (No. U1931209) and National Key R&D Program of China(No. 2019YFA0405502). Guoshoujing Telescope (the Large Sky Area Multi-Object Fiber Spectroscopic Telescope, LAMOST) is a National Major Scientific Project built by the Chinese Academy of Sciences. Funding for the project has been provided by the National Development and Reform Commission. LAMOST is operated and managed by the National Astronomical Observatories, Chinese Academy of Sciences. Siqi Liu thanks the useful discussion with Sophia Y. Dai, Qing Liu, Er-Lin Qiao and He-Yang Liu. This research uses Astropy,⁵ (Astropy Collaboration et al. 2013, 2018), TOPCAT (Taylor 2005), Scipy (Virtanen et al. 2020), Numpy (Harris et al. 2020) and Matplotlib (Hunter 2007)

⁴ <https://doi.org/10.12149/101085>

⁵ <http://www.astropy.org>

REFERENCES

- Ahumada, R., Prieto, C. A., Almeida, A., et al. 2020, *ApJS*, 249, 3, doi: [10.3847/1538-4365/ab929e](https://doi.org/10.3847/1538-4365/ab929e)
- Allende Prieto, C., Lambert, D. L., & Asplund, M. 2001, *ApJL*, 556, L63, doi: [10.1086/322874](https://doi.org/10.1086/322874)
- Astropy Collaboration, Robitaille, T. P., Tollerud, E. J., et al. 2013, *A&A*, 558, A33, doi: [10.1051/0004-6361/201322068](https://doi.org/10.1051/0004-6361/201322068)
- Astropy Collaboration, Price-Whelan, A. M., Sipőcz, B. M., et al. 2018, *AJ*, 156, 123, doi: [10.3847/1538-3881/aabc4f](https://doi.org/10.3847/1538-3881/aabc4f)
- Baldry, I. K., Glazebrook, K., Brinkmann, J., et al. 2004, *ApJ*, 600, 681, doi: [10.1086/380092](https://doi.org/10.1086/380092)
- Baldwin, J. A., Phillips, M. M., & Terlevich, R. 1981, *PASP*, 93, 5, doi: [10.1086/130766](https://doi.org/10.1086/130766)
- Bauer, A. E., Drory, N., Hill, G. J., & Feulner, G. 2005, *ApJL*, 621, L89, doi: [10.1086/429289](https://doi.org/10.1086/429289)
- Bianchi, L., Shiao, B., & Thilker, D. 2017, *ApJS*, 230, 24, doi: [10.3847/1538-4365/aa7053](https://doi.org/10.3847/1538-4365/aa7053)
- Bianchi, L., Shiao, B., & Thilker, D. 2017, *The Astrophysical Journal Supplement Series*, 230, 24, doi: [10.3847/1538-4365/aa7053](https://doi.org/10.3847/1538-4365/aa7053)
- Blanton, M. R., Bershadsky, M. A., Abolfathi, B., et al. 2017, *AJ*, 154, 28, doi: [10.3847/1538-3881/aa7567](https://doi.org/10.3847/1538-3881/aa7567)
- Boquien, M., Burgarella, D., Roehlly, Y., et al. 2019, *A&A*, 622, A103, doi: [10.1051/0004-6361/201834156](https://doi.org/10.1051/0004-6361/201834156)
- Brinchmann, J., Charlot, S., White, S. D. M., et al. 2004, *MNRAS*, 351, 1151, doi: [10.1111/j.1365-2966.2004.07881.x](https://doi.org/10.1111/j.1365-2966.2004.07881.x)
- Borby, M., Kaaret, P., Prestwich, A., & Mirabel, I. F. 2016, *MNRAS*, 457, 4081, doi: [10.1093/mnras/stw284](https://doi.org/10.1093/mnras/stw284)
- Brunker, S. W., Salzer, J. J., Janowiecki, S., Finn, R. A., & Helou, G. 2020, *ApJ*, 898, 68, doi: [10.3847/1538-4357/ab9ec0](https://doi.org/10.3847/1538-4357/ab9ec0)
- Bruzual, G., & Charlot, S. 2003, *Monthly Notices of the Royal Astronomical Society*, 344, 1000
- Bruzual, G., & Charlot, S. 2003, *MNRAS*, 344, 1000, doi: [10.1046/j.1365-8711.2003.06897.x](https://doi.org/10.1046/j.1365-8711.2003.06897.x)
- Burgarella, D., Buat, V., & Iglesias-Páramo, J. 2005, *MNRAS*, 360, 1413, doi: [10.1111/j.1365-2966.2005.09131.x](https://doi.org/10.1111/j.1365-2966.2005.09131.x)
- Calzetti, D., Armus, L., Bohlin, R. C., et al. 2000, *The Astrophysical Journal*, 533, 682
- Calzetti, D., Armus, L., Bohlin, R. C., et al. 2000, *ApJ*, 533, 682, doi: [10.1086/308692](https://doi.org/10.1086/308692)
- Cardamone, C., Schawinski, K., Sarzi, M., et al. 2009, *MNRAS*, 399, 1191, doi: [10.1111/j.1365-2966.2009.15383.x](https://doi.org/10.1111/j.1365-2966.2009.15383.x)
- Casey, C. M. 2012, *MNRAS*, 425, 3094, doi: [10.1111/j.1365-2966.2012.21455.x](https://doi.org/10.1111/j.1365-2966.2012.21455.x)
- Chabrier, G. 2003, *PASP*, 115, 763, doi: [10.1086/376392](https://doi.org/10.1086/376392)
- Cherinka, B., Andrews, B. H., Sánchez-Gallego, J., et al. 2019, *AJ*, 158, 74, doi: [10.3847/1538-3881/ab2634](https://doi.org/10.3847/1538-3881/ab2634)
- Chilingarian, I. V., Melchior, A.-L., & Zolotukhin, I. Y. 2010, *MNRAS*, 405, 1409, doi: [10.1111/j.1365-2966.2010.16506.x](https://doi.org/10.1111/j.1365-2966.2010.16506.x)
- Chilingarian, I. V., & Zolotukhin, I. Y. 2012, *MNRAS*, 419, 1727, doi: [10.1111/j.1365-2966.2011.19837.x](https://doi.org/10.1111/j.1365-2966.2011.19837.x)
- Cid Fernandes, R., Mateus, A., Sodré, L., Stasińska, G., & Gomes, J. M. 2005, *MNRAS*, 358, 363, doi: [10.1111/j.1365-2966.2005.08752.x](https://doi.org/10.1111/j.1365-2966.2005.08752.x)
- Cui, X.-Q., Zhao, Y.-H., Chu, Y.-Q., et al. 2012, *Research in Astronomy and Astrophysics*, 12, 1197, doi: [10.1088/1674-4527/12/9/003](https://doi.org/10.1088/1674-4527/12/9/003)
- Dopita, M. A. 2005, in *American Institute of Physics Conference Series*, Vol. 761, *The Spectral Energy Distributions of Gas-Rich Galaxies: Confronting Models with Data*, ed. C. C. Popescu & R. J. Tuffs, 203–222, doi: [10.1063/1.1913931](https://doi.org/10.1063/1.1913931)
- Dopita, M. A., & Ryder, S. D. 1994, *ApJ*, 430, 163, doi: [10.1086/174390](https://doi.org/10.1086/174390)
- Du, B., Luo, A. L., Kong, X., et al. 2016, *ApJS*, 227, 27, doi: [10.3847/1538-4365/227/2/27](https://doi.org/10.3847/1538-4365/227/2/27)
- Fazio, G. G., Hora, J. L., Allen, L. E., et al. 2004, *ApJS*, 154, 10, doi: [10.1086/422843](https://doi.org/10.1086/422843)
- Fritz, J., Franceschini, A., & Hatziminaoglou, E. 2006, *MNRAS*, 366, 767, doi: [10.1111/j.1365-2966.2006.09866.x](https://doi.org/10.1111/j.1365-2966.2006.09866.x)
- Fukugita, M., Ichikawa, T., Gunn, J. E., et al. 1996, *AJ*, 111, 1748, doi: [10.1086/117915](https://doi.org/10.1086/117915)
- Gao, Y.-L., Lian, J.-H., Kong, X., et al. 2017, *Research in Astronomy and Astrophysics*, 17, 041, doi: [10.1088/1674-4527/17/5/41](https://doi.org/10.1088/1674-4527/17/5/41)
- Hao, C.-N., Kennicutt, R. C., Johnson, B. D., et al. 2011, *ApJ*, 741, 124, doi: [10.1088/0004-637X/741/2/124](https://doi.org/10.1088/0004-637X/741/2/124)
- Harish, S., Malhotra, S., Rhoads, J. E., et al. 2021, *arXiv e-prints*, arXiv:2105.13400, <https://arxiv.org/abs/2105.13400>
- Harris, C. R., Millman, K. J., van der Walt, S. J., et al. 2020, *Nature*, 585, 357, doi: [10.1038/s41586-020-2649-2](https://doi.org/10.1038/s41586-020-2649-2)
- Hinshaw, G., Larson, D., Komatsu, E., et al. 2013, *ApJS*, 208, 19, doi: [10.1088/0067-0049/208/2/19](https://doi.org/10.1088/0067-0049/208/2/19)
- Hunter, J. D. 2007, *Computing in Science & Engineering*, 9, 90, doi: [10.1109/MCSE.2007.55](https://doi.org/10.1109/MCSE.2007.55)
- Izotov, Y. I., Guseva, N. G., & Thuan, T. X. 2011, *ApJ*, 728, 161, doi: [10.1088/0004-637X/728/2/161](https://doi.org/10.1088/0004-637X/728/2/161)
- Izotov, Y. I., Stasińska, G., Meynet, G., Guseva, N. G., & Thuan, T. X. 2006, *A&A*, 448, 955, doi: [10.1051/0004-6361:20053763](https://doi.org/10.1051/0004-6361:20053763)
- Jarrett, T. H., Cohen, M., Masci, F., et al. 2011, *ApJ*, 735, 112, doi: [10.1088/0004-637X/735/2/112](https://doi.org/10.1088/0004-637X/735/2/112)

- Jiang, T., Malhotra, S., Rhoads, J. E., & Yang, H. 2019, *ApJ*, 872, 145, doi: [10.3847/1538-4357/aaee8a](https://doi.org/10.3847/1538-4357/aaee8a)
- Kauffmann, G., Heckman, T. M., Tremonti, C., et al. 2003, *MNRAS*, 346, 1055, doi: [10.1111/j.1365-2966.2003.07154.x](https://doi.org/10.1111/j.1365-2966.2003.07154.x)
- Kennicutt, Robert C., J. 1998, *ARA&A*, 36, 189, doi: [10.1146/annurev.astro.36.1.189](https://doi.org/10.1146/annurev.astro.36.1.189)
- Kennicutt, R. C., & Evans, N. J. 2012, *ARA&A*, 50, 531, doi: [10.1146/annurev-astro-081811-125610](https://doi.org/10.1146/annurev-astro-081811-125610)
- Kewley, L. J., Dopita, M. A., Sutherland, R. S., Heisler, C. A., & Trevena, J. 2001, *ApJ*, 556, 121, doi: [10.1086/321545](https://doi.org/10.1086/321545)
- Kewley, L. J., Groves, B., Kauffmann, G., & Heckman, T. 2006, *MNRAS*, 372, 961, doi: [10.1111/j.1365-2966.2006.10859.x](https://doi.org/10.1111/j.1365-2966.2006.10859.x)
- Koenig, X. P., & Leisawitz, D. T. 2014, *ApJ*, 791, 131, doi: [10.1088/0004-637X/791/2/131](https://doi.org/10.1088/0004-637X/791/2/131)
- Luo, A. L., Zhang, H.-T., Zhao, Y.-H., et al. 2012, *Research in Astronomy and Astrophysics*, 12, 1243, doi: [10.1088/1674-4527/12/9/004](https://doi.org/10.1088/1674-4527/12/9/004)
- Maitra, C., Haberl, F., Ivanov, V. D., Cioni, M.-R. L., & van Loon, J. T. 2019, *A&A*, 622, A29, doi: [10.1051/0004-6361/201833663](https://doi.org/10.1051/0004-6361/201833663)
- Marino, R. A., Rosales-Ortega, F. F., Sánchez, S. F., et al. 2013, *A&A*, 559, A114, doi: [10.1051/0004-6361/201321956](https://doi.org/10.1051/0004-6361/201321956)
- Martin, D. C., Fanson, J., Schiminovich, D., et al. 2005, *ApJL*, 619, L1, doi: [10.1086/426387](https://doi.org/10.1086/426387)
- Mateus, A., Sodr , L., Cid Fernandes, R., et al. 2006, *MNRAS*, 370, 721, doi: [10.1111/j.1365-2966.2006.10565.x](https://doi.org/10.1111/j.1365-2966.2006.10565.x)
- Mineo, S., Gilfanov, M., & Sunyaev, R. 2012, *MNRAS*, 419, 2095, doi: [10.1111/j.1365-2966.2011.19862.x](https://doi.org/10.1111/j.1365-2966.2011.19862.x)
- Murphy, E. J., Condon, J. J., Schinnerer, E., et al. 2011, *ApJ*, 737, 67, doi: [10.1088/0004-637X/737/2/67](https://doi.org/10.1088/0004-637X/737/2/67)
- Noll, S., Burgarella, D., Giovannoli, E., et al. 2009, *A&A*, 507, 1793, doi: [10.1051/0004-6361/200912497](https://doi.org/10.1051/0004-6361/200912497)
- Oke, J. B., & Gunn, J. E. 1983, *ApJ*, 266, 713, doi: [10.1086/160817](https://doi.org/10.1086/160817)
- Panuzzo, P., Bressan, A., Granato, G. L., Silva, L., & Danese, L. 2003, *A&A*, 409, 99, doi: [10.1051/0004-6361:20031094](https://doi.org/10.1051/0004-6361:20031094)
- Pettini, M., & Pagel, B. E. J. 2004, *MNRAS*, 348, L59, doi: [10.1111/j.1365-2966.2004.07591.x](https://doi.org/10.1111/j.1365-2966.2004.07591.x)
- Rieke, G. H., Young, E. T., Engelbracht, C. W., et al. 2004, *ApJS*, 154, 25, doi: [10.1086/422717](https://doi.org/10.1086/422717)
- Speagle, J. S., Steinhardt, C. L., Capak, P. L., & Silverman, J. D. 2014, *ApJS*, 214, 15, doi: [10.1088/0067-0049/214/2/15](https://doi.org/10.1088/0067-0049/214/2/15)
- Su, D.-Q., & Cui, X.-Q. 2004, *ChJA&A*, 4, 1, doi: [10.1088/1009-9271/4/1/1](https://doi.org/10.1088/1009-9271/4/1/1)
- Taylor, M. B. 2005, in *Astronomical Society of the Pacific Conference Series*, Vol. 347, *Astronomical Data Analysis Software and Systems XIV*, ed. P. Shopbell, M. Britton, & R. Ebert, 29
- Thomas, D., Steele, O., Maraston, C., et al. 2013, *MNRAS*, 431, 1383, doi: [10.1093/mnras/stt261](https://doi.org/10.1093/mnras/stt261)
- Traulsen, I., Schwobe, A. D., Lamer, G., et al. 2020, *A&A*, 641, A137, doi: [10.1051/0004-6361/202037706](https://doi.org/10.1051/0004-6361/202037706)
- Tremonti, C. A., Heckman, T. M., Kauffmann, G., et al. 2004, *ApJ*, 613, 898, doi: [10.1086/423264](https://doi.org/10.1086/423264)
- van Zee, L., Salzer, J. J., Haynes, M. P., O'Donoghue, A. A., & Balonek, T. J. 1998, *AJ*, 116, 2805, doi: [10.1086/300647](https://doi.org/10.1086/300647)
- Veilleux, S., & Osterbrock, D. E. 1987, *ApJS*, 63, 295, doi: [10.1086/191166](https://doi.org/10.1086/191166)
- Virtanen, P., Gommers, R., Oliphant, T. E., et al. 2020, *Nature Methods*, 17, 261, doi: [10.1038/s41592-019-0686-2](https://doi.org/10.1038/s41592-019-0686-2)
- Wang, L.-L., Luo, A. L., Shen, S.-Y., et al. 2018, *MNRAS*, 474, 1873, doi: [10.1093/mnras/stx2798](https://doi.org/10.1093/mnras/stx2798)
- Wang, S.-G., Su, D.-Q., Chu, Y.-Q., Cui, X., & Wang, Y.-N. 1996, *ApOpt*, 35, 5155, doi: [10.1364/AO.35.005155](https://doi.org/10.1364/AO.35.005155)
- Webb, N. A., Coriat, M., Traulsen, I., et al. 2020, *A&A*, 641, A136, doi: [10.1051/0004-6361/201937353](https://doi.org/10.1051/0004-6361/201937353)
- Werner, M. W., Roellig, T. L., Low, F. J., et al. 2004, *ApJS*, 154, 1, doi: [10.1086/422992](https://doi.org/10.1086/422992)
- Wright, E. L., Eisenhardt, P. R. M., Mainzer, A. K., et al. 2010, *AJ*, 140, 1868, doi: [10.1088/0004-6256/140/6/1868](https://doi.org/10.1088/0004-6256/140/6/1868)
- Xue, Y. Q., Luo, B., Brandt, W. N., et al. 2011, *ApJS*, 195, 10, doi: [10.1088/0067-0049/195/1/10](https://doi.org/10.1088/0067-0049/195/1/10)
- Yang, H., Malhotra, S., Rhoads, J. E., & Wang, J. 2017, *ApJ*, 847, 38, doi: [10.3847/1538-4357/aa8809](https://doi.org/10.3847/1538-4357/aa8809)
- Zhao, G., Zhao, Y.-H., Chu, Y.-Q., Jing, Y.-P., & Deng, L.-C. 2012, *Research in Astronomy and Astrophysics*, 12, 723, doi: [10.1088/1674-4527/12/7/002](https://doi.org/10.1088/1674-4527/12/7/002)